JOURNAL OF GUIDANCE, CONTROL, AND DYNAMICS
Vol. 15, No. 4, July-August 1992

X-29 H_∞ Controller Synthesis

W. L. Rogers* and D. J. Collins†
Naval Postgraduate School, Monterey, California 93943

H_2 and H_∞ controllers have been designed for the unstable longitudinal analog backup mode of the X-29 aircraft. When actuator design limitations are considered, the expected superiority of the H_∞ design over the H_2 design is not obtained. The limited performance designs also do not exhibit the precision flight-path control modes that are characteristic of the H_∞ designs.

I. Introduction

A CHALLENGING application of H_∞ control theory is the synthesis of a stabilizing controller for the longitudinal dynamics of the X-29. The X-29 is a technology demonstrator with a unique forward-swept wing design that offers the advantages of improved maneuverability, better low-speed handling, and reduced stall speeds. The X-29's longitudinal dynamics are designed with 35% negative static stability margin. Unlike the advanced figther model with an unstable phugoid mode used by Chaing and Safonov[1] to demonstrate H_2 and H_∞ methodology, the X-29 has an unstable short period mode, i.e., a real pole on the positive axis.

The X-29 controller synthesis was performed using Pro-Matlab and the Matlab Robust-Control Tool Box software. These application packages were run on a Sun 386i workstation. The script files specifically written or modified for this problem and all matrices not listed in this article as well as additional singular value plots are given in Rogers.[2]

The paper discusses the X-29 state-space model, the H_∞ design objectives and specifications, the controller synthesis, and the design results including the aircraft's longitudinal responses to test inputs. Design limitations due to the actuator performance are investigated in an alternate controller.

II. X-29 Model Description

The X-29 longitudinal dynamics model is that of the aircraft's analog reversion mode with the aircraft trimmed at 0.5 Mach, 30,000 ft. An 83rd-order model[3] was reduced to a 14 state model that includes a short-period approximation of the aircraft longitudinal dynamics, vertical velocity w and pitch rate q, and fourth-order actuator dynamics for each of the three longitudinal control surfaces, i.e., the canards, flaps, and strakes. Eliminated from the 83rd-order model were the flexible mode dynamics, aerodynamic lag terms, sensor dynamics, and notch filter.

Figure 1 presents the physical configuration of the open-loop actuator/aircraft dynamics model. Some of the actuator gains shown in Fig. 1 may have changed in the current aircraft configuration. For the purposes of this study, two separate commands, r_1 and r_2, are input to the three control surface actuators with r_1 controlling the canards and r_2 controlling the flaps and strakes. Although not truly representative of the X-29, this configuration provides multiple, independently controlled surfaces representative of a supermaneuverable aircraft. As will be seen, this configuration results in the synthesis of advanced control modes that are characteristic of supermaneuverable aircraft designs. The control inputs to the aircraft dynamics are the canards δ_c, the flaps δ_f, the strakes δ_s, and their respective first and second derivatives. The measured outputs are the two aircraft states, w and q. Thus, the model has two inputs, two outputs and 14 states.

The 14th-order model was scaled to improve the numerical conditioning of its state-space representation. In the scaling process, the w state was transformed to angle of attack α, i.e., $\alpha = w/U_0$ where U_0 is the initial forward velocity, and the units of the actuator third derivative states were transformed from rad/s^3 to 1E+04 rad/s^3. This scaling was effective in reducing the condition number of the system's A matrix from an order of magnitude of 10^{10} to 10^4.

From the state-space realization of the resultant 14-state linear model, the plant transfer matrix was calculated by $G(s) = C(sI - A)^{-1}B + D$. The open-loop poles of the X-29 model are listed in Table 1. Note that the unstable short-period mode has a real pole at 1.9550.

The singular-value plot of the X-29 return difference matrix $I + G(s)$ is presented in Fig. 2 where the solid upper curve is $\sigma_{\max}[I + G(jw)]$ and the dashed lower curve is $\sigma_{\min}[I + G(jw)]$. The inverse of the return difference matrix is called the sensitivity matrix $S(s)$, which is discussed in the next section. Some design procedures, although expressed in terms of the $S(s)$ sensitivity matrix, may be more clearly illustrated by plots of the return difference matrix.

III. Design Objectives

The design procedure followed in the development of the H_∞ controller was to suppress as much as possible the system sensitivity matrix $S(s)$ through variation of a weighting matrix W_1. The weighting matrix W_1 includes a constant parameter γ. As γ is increased from one design to another, $S(s)$ is suppressed. The relationship of the weighting matrix and the sensitivity matrix will become clearer in the discussion of the H_∞ theory given below [Eq. (1)]. The decrease in size or suppression of the $S(s)$ matrix is shown by plotting the singular values of the matrix [as a function of ω as in Fig. 2 for the return difference matrix.] These singular value plots are called Sigma plots.

This method of approach is essentially an extension of classical design procedures to multi-input-multi-output (MIMO) problems. In classical design, high gains can lead to good

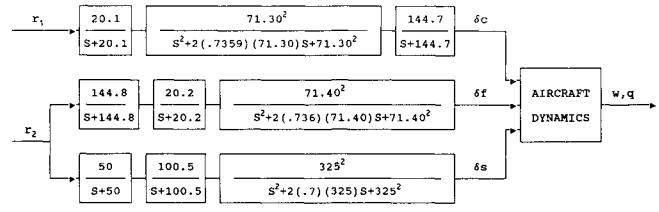

Fig. 1 X-29 actuator/aircraft configuration.

Received July 5, 1990; revision received March 6, 1991; accepted for publication March 18, 1991. This paper is declared a work of the U.S. Government and is not subject to copyright protection in the United States.

*Lieutenant Commander, U.S. Navy.
†Professor of Aeronautics AA/CO, Aeronautics and Astronautics Department.

performance with minimization of plant disturbances and plant uncertainty due to the suppression of the sensitivity function. The suppression of the sensitivity function is illustrated by Bode plots of $S(s)$. In the case of MIMO analysis, Sigma plots replace Bode plots in the analysis.

A fixed robustness constraint that limits the bandwidth of the closed-loop transfer matrix is obtained by applying a weighting matrix W_3 to the complementary sensitivity matrix $T(s)$ which can be expressed as $T(s)=I-S(s)$. As the sensitivity matrix is suppressed, $T(s)$ approaches I and its bandwidth increases to the fixed limit $1/W_3$. By the selection of W_3, a prescribed dropout at higher frequencies can also be imposed on the closed-loop transfer matrix.

Finally, a fixed weighting matrix W_2 on the control input to the plant can be used to limit the size of the controller gain matrix $F(s)$. In the designs considered below, W_2 was varied in order to meet the physical constraints introduced by the actuators. The H_∞ infinity theory methodology insures that $F(s)$ stabilizes the augmented plant matrix.

We now define the weighting matrices used in this study, and give a brief outline of the H_∞ theory. The outline shows how the weighting matrices and the sensitivity matrix, complementary sensitivity, and gain matrices are related through the H_∞ norm of the closed-loop transfer matrix $T_{y_1 u_1}$.

In this problem, it is necessary to attenuate the closed-loop singular values of the complementary sensitivity matrix $\sigma_i[T(jw)]$ by 20 dB at frequencies beyond 100 rad/s, and to exhibit a second-order rolloff beyond 100 rad/s. These stability requirements ensure that the X-29 system has sufficient stability margin to tolerate modeling errors or loop transfer function variations that could arise from the unmodeled flexible modes. The flexible modes are observed in the Bode plot of the 83rd-order X-29 model at the frequencies 100–250 rad/s. The specified second-order rolloff also closely matches that of the open-loop plant.

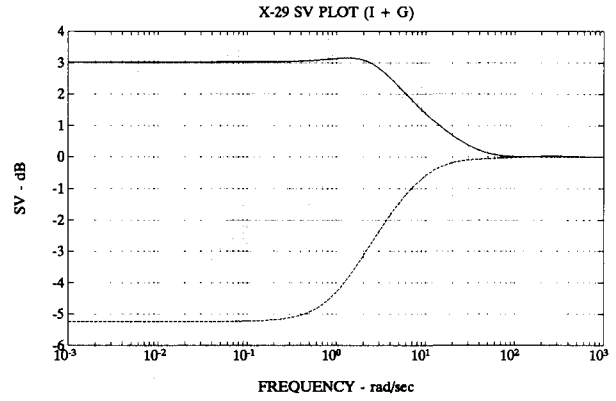

Fig. 2 Uncompensated return difference singular values.

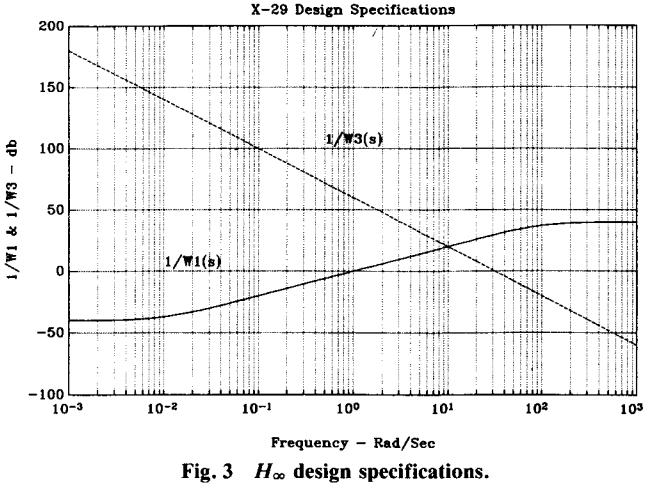

Fig. 3 H_∞ design specifications.

Table 1 Uncompensated X-29 open-loop poles[a]

1.9550E+00	−2.7155E+00
−2.2746E+02 ± 2.3201E+02i	−1.4491E+02
−5.2506E+01 ± 4.8410E+01i	−1.4455E+02
−5.2518E+01 ± 4.8255E+01i	−1.0031E+02
−5.0067E+01	−2.0172E+01
−2.0115E+01	

[a]The uncompensated X-29 model is unstable.

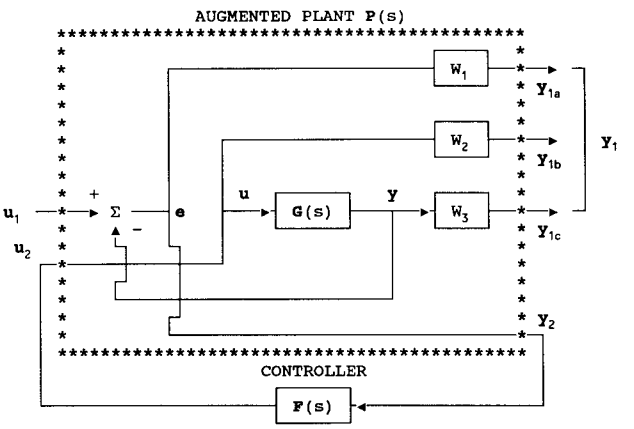

Fig. 4 Augmented plant and controller standard form.

The following $(\gamma W_1)^{-1}(s)$, $W_2(s)$, and $W_3^{-1}(s)$ weighting functions were selected to meet the above performance objectives and stability constraints:

$$(\gamma W_1)^{-1}(s) = \gamma^{-1}\left[0.01(100s+1)/0.01s+1\right]I_{(2\times 2)} \tag{1}$$

$$W_2(s) = -0.001 I_{(4\times 4)} \tag{2}$$

$$W_3^{-1}(s) = (1000/s^2) I_{(2\times 2)} \tag{3}$$

A plot of the H_∞ $W_1^{-1}(s)$ and $W_3^{-1}(s)$ weighting functions is shown in Fig. 3. The standard formulation of an H_∞ requires the development of an augmented plant matrix $P(s)$

$$P(s) = \left[\begin{array}{c|c} W_1 & -W_1 G \\ 0 & W_2 \\ 0 & W_3 G \\ \hline I & -G \end{array}\right] \tag{4}$$

Although performance specifications are given in the frequency domain, all calculations are done in the state representation or the time domain. The state-space representation of $P(s)$ is given in Eq. (5)

$$P(s) = \left[\begin{array}{c|cc} A & B_1 & B_2 \\ \hline C_1 & D_{11} & D_{12} \\ C_2 & D_{21} & D_{22} \end{array}\right] \tag{5}$$

The relationship of the weighting matrices and the plant matrix $G(s)$ to $P(s)$ is shown in Fig. 4. The $W_2(s)$ weighting is included to ensure that the D_{12} submatrix of state-space representation of the augmented plant $P(s)$ has full column rank. This weighting function (as shown in the figure) penalizes the control u input to the X-29 plant $G(s)$ and thus eliminates solutions based on infinite impulses. As the $W_3(s)$ weighting function is not proper, it has no state-space realization. However, the term $W_3(s)G(s)$ of the augmented plant $P(s)$ is proper and can be realized in the required state-space form.

The closed-loop transfer function matrix can be expressed in terms of the partitioned $P(s)$ matrix and the to-be-determined feedback matrix $F(s)$ as

$$T_{y1u1} = P_{11}(s) + P_{12}(s)\left[I - F(s)P_{22}(s)\right]^{-1}F(s)P_{21}(s) \quad (6)$$

The H_∞ theory requires that the norm of closed-loop transfer function be less than one:

$$\|T_{y_1u_1}\|_\infty \leq 1 \quad (7)$$

The norm can also be expressed in terms of the sensitivity, complementary sensitivity, and gain matrices with the appropriate weighting matrices as

$$T_{y_1u_1} :: \begin{bmatrix} W_1S \\ W_2FS \\ W_3T \end{bmatrix} \quad (8)$$

where $S(s)$ is the sensitivity matrix and $T(s)$ is the complementary sensitivity. This representation indicates why performance specifications are given in terms of $S(s)$ and $T(s)$ and why $W_1(s)$ is the performance weighting and $W_3(s)$ is the robustness weighting. As indicated, the $W_2(s)$ weighting limits the values of the controller gains $F(s)$.

The resultant X-29 augmented plant $P(s)$ is an 16th-order system with $W_1(s)$ adding two states to the X-29 plant $G(s)$. The $W_3(s)$ function does not add states to $G(s)$ as a state-space realization of this function does not exist. Using the two Riccati solution method, H_2 and H_∞ synthesized controllers are the same size as the augmented plant $P(s)$. As such, the final X-29 controller is expected to be of 16th order.

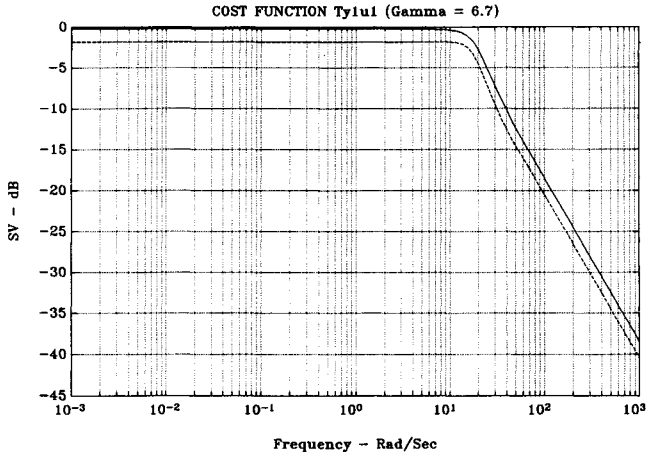

Fig. 5 H_2 $T_{y_1u_1}$ **singular values.**

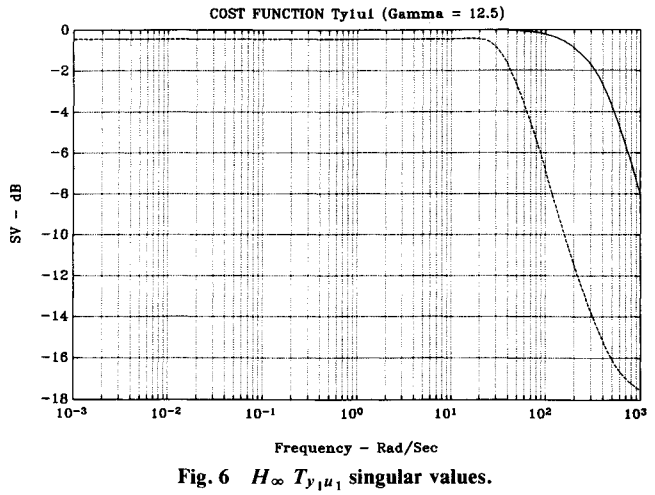

Fig. 6 H_∞ $T_{y_1u_1}$ **singular values.**

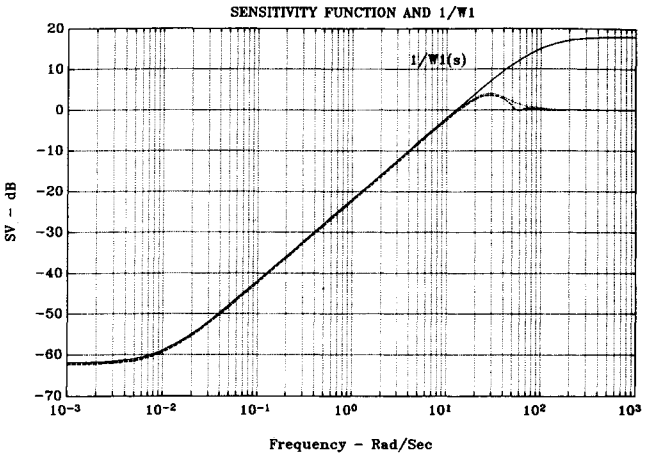

Fig. 7 Sensitivity $S(s)$ (H_∞, $\gamma = 12.5$).

IV. Controller Synthesis

The controller synthesis began with the development of an H_2 solution to obtain an initial indication of achievable performance levels. To insure a well-posed H_2 problem, the upper corner frequncy of the $W_1^{-1}(s)$ weighting function was removed by making the denominator of $W_1^{-1}(s)$ a constant value. This insured that the D_{11} submatrix of the state-space representation of the augmented plant $P(s)$ is zero as is required by H_2 control theory.

Solutions to the H_2 and the H_∞ small-gain problems were obtained for increasing values of γ until 1) for the H_2 solution, the cost function $\|T_{y1u1}\|_2$ reached the "all pass limit," i.e., 0 dB; and 2) for the H_∞ solution, no stabilizing controller satisfied the H_∞ small-gain problem for a larger value of γ, i.e., no solution existed for a larger γ.

Figure 5 contains Sigma plots of the $\sigma_{\max}$ (solid upper curve) and $\sigma_{\min}$ (dotted lower curve) of the H_2 transfer matrix T_{y1u1} for a γ value of 6.7, and Fig. 6 that of the H_∞ transfer matrix T_{y1u1} for a γ value of 12.5. Since the largest gain of the system is bounded above by $\sigma_{\max}$ and the smallest gain is bounded below by $\sigma_{\min}$, the actual performance of the system is confined between the two bounds.

The H_2 solution pushes both singular values to within 2 dB of the "all pass limit." However, with a maximum γ of 12.5, the H_∞ solution pushes the T_{y1u1} singular values to within 0.5 dB of the "all pass limit," and the solution also has a larger bandwidth. The significantly larger value of γ in the H_∞ solution indicates that a higher level of performance is achieved with the H_∞ solution compared to that reached by the H_2 solution.

Figure 7 contains singular-value plots of the sensitivity matrix $S(s)$ and $(\gamma W_1)^{-1}(s)$ weighting function for the H_∞ solution with a γ of 12.5, respectively. The solid curve is $1/W_1$ while the dotted curve is $\sigma_{\max}[S(jw)]$ and the dashed lower curve is $\sigma_{\min}[S(jw)]$. Figure 8 has singular-value plots of the complementary sensitivity matrix $T(s)$ and $W_3^{-1}(s)$ weighting function for the H_∞ solution with a γ of 12.5. Here, the dashed upper curve is $\sigma_{\max}[T(jw)]$ while the dotted lower curve is $\sigma_{\min}[T(jw)]$. As γ is increased from 1 to 12.5, the sensitivity function $S(s)$ is incrementally suppressed by the $(\gamma W_1)^{-1}(s)$ weighting function, and the complementary sensitivity function $T(s)$ is pushed toward the stability constraint, i.e., the $S(s)$ and $T(s)$ singular values are forced against their respective limits $(\gamma W_1)^{-1}(s)$ and $W_3^{-1}(s)$. The H_∞ compensated X-29 is characterized by larger disturbance attenuation, lower sensitivity to plant variations and modeling errors, and a wide control bandwidth ω_B. The closed-loop bandwidth of the H_∞ solution is nearly 30 rad/s.

The H_∞ solution to the small-gain problem results in an 18th-order controller. A minimal realization was performed to eliminate two uncontrollable and unobservable states. Next, the minimal 16th-order controller was balanced to improve the

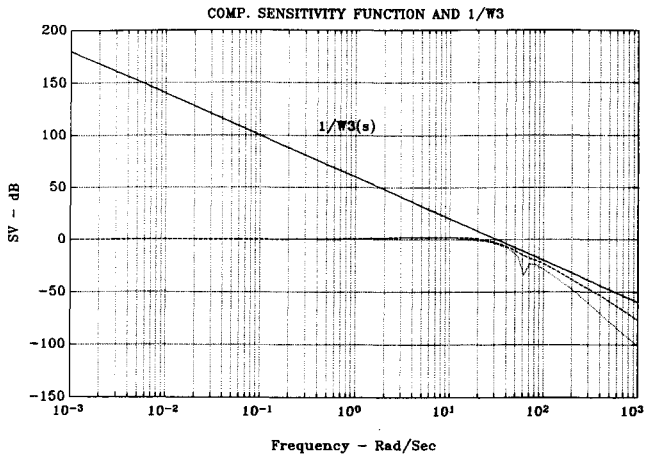

Fig. 8 Complementary sensitivity $T(s)$ (H_∞, $\gamma = 12.5$).

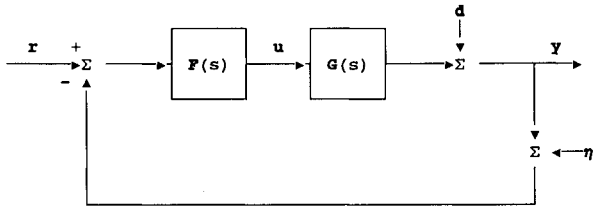

Fig. 9 Controller and plant.

numerical conditioning of the controller model. The resultant 16th-order minimal controller was used in plotting the singular values of T_{y1u1}, the sensitivity function $S(s)$, and the complementary sensitivity function $T(s)$ results presented in previous figures.

V. Design Results of the H_∞ Controller

The closed-loop configuration of the H_∞ compensated X-29 is presented in Fig. 9, where $F(s)$ and $G(s)$ are the 16th-order controller and 14th-order X-29 plant transfer function matrices, respectively.

The output vector y is made up of the aircraft states α and q, and the command vector r is composed of separate command elements r_1 and r_2. Unlike the open-loop actuator/aircraft dynamics model presented in Fig. 1, r_1 and r_2 are reference commands to the controlled outputs, α and q. This is a result of the controller being placed in series with the X-29 plant in the feedforward loop and the negative unity feedback. Thus the closed-loop, compensated X-29 model has two inputs, two outputs and 30 states. As will be seen, this closed-loop configuration still provides the multiple, independently controlled surfaces observed with the open-loop, uncompensated X-29 plant $G(s)$.

A balanced realization of the separate state-space representation of the controller $F(s)$ and the X-29 plant $G(s)$ was obtained to improve their numerical conditioning. As a result of this balancing, the internal structures of $F(s)$ and $G(s)$ were altered making identification of the individual states difficult. It is interesting to note that the unstable short-period pole of the open-loop system is mirrored into the left half-plane of the closed-loop system, i.e., -1.9550. This is not a coincidence as an identical occurrence is observed in Safonov's advanced fighter example presented in Ref. 1. In Safonov's example, the unstable phugoid poles of the advanced fighter's open-loop model are mirrored into the left half-plane of the compensated, closed-loop model. This mirror imaging can represent a basic limitation to the system's performance if, as in the case of the compensated X-29, this is the dominant pole unless some precontroller is introduced.

The singular values of the return difference and inverse-return difference matrices quantify a system's feedback properties. In the following paragraphs, the feedback properties of the H_∞ compensated X-29 will be measured using singular-value plots of its return difference matrices.

The singular-value plots of the compensated X-29 output, return difference matrices is presented in Fig. 10. Comparison should be made with the similar plot for the uncompensated plant in Fig. 2. The output return difference matrix $I + G(s)F(s)$ (also referred to as the output, additive return difference matrix) is the inverse of the sensitivity matrix $S(s)$. The minimum singular value of this return difference matrix approximates the loop gain whenever the loop gains are large, i.e., $G(s)F(s)$. Figure 2 indicated that the uncompensated X-29 possesses small loop gains along with the corresponding traits of poor disturbance attenuation and high sensitivity to plant variations and modeling errors. Figure 10 shows how the H_∞ synthesized controller has markedly improved the X-29 performance properties. The large loop gains indicate good disturbance attenuation and low sensitivity to uncertainties over a control bandwidth ω_B of approximately 9 rad/s. However, the drop of the singular values below the 0-dB line indicates that performance is lacking near the 0-dB crossover frequency. This is probably caused by the steep rolloff (-40 dB/decade) designed into the complementary sensitivity function. Finally, the 9 rad/s control bandwidth ω_B of the compensated X-29 is less than the multiplicative robust frequency ω_{rm} of 30 rad/s, insuring that one of the required condition for stability is not violated at the X-29 plant output.

The minimum singular value of the output inverse-return difference matrix $\sigma_{\min}[I + (G(j\omega)(F(j\omega))]^{-1}$ can provide a measure of the aircraft's gain and phase margins with respect to multiplicative modeling errors using the universal gain and phase margin curve.[4] The minimum singular value $\sigma_{\min}[I + (G(j\omega)(F(j\omega))^{-1}]$ drops to approximately -2 dB at frequencies between 1 rad/s and 20 rad/s. The gain and phase margins of the compensated X-29 near the 0-dB crossover frequency are thus -14 dB to $+5$ dB and ± 47 deg. This is more stable than the -8 dB to $+4$ dB, ± 35-deg gain, and phase margins typically designed into a fighter aircraft.

The closed-loop, compensated X-29 model (Fig. 9) exhibits precision flight-path control modes as a result of the multiple, independently controlled surface configuration. The three precision longitudinal modes observed are as follows:

1) Vertical translation: The aircraft vertical velocity is controlled at a constant θ by varying α, i.e., the aircraft flight-path angle γ or velocity vector is controlled while x_s remains fixed.

2) Direct lift control: The aircraft flight-path angle γ is controlled at a constant α by varying θ, i.e., the aircraft flight-path angle γ or velocity vector remains along the aircraft stability axis x_s as x_s rotates.

3) Pitch pointing: The aircraft pitch attitude θ is controlled at a constant flight-path angle γ, i.e., the aircraft flight-path angle γ or velocity vector remains fixed while x_s rotates ($\theta = \alpha$).

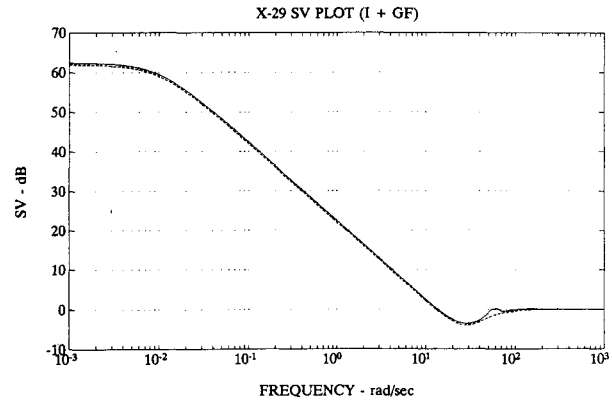

Fig. 10 Compensated return difference values ($\gamma = 12.5$).

A pulse input of 1 deg was applied separately for 1 s to each of the two reference commands to judge the performance of the controller. Following standard convention, a positive α or q corresponds to a nose-up response, and a positive control deflection is trailing edge down for all three control surfaces. Positive canard deflection δ_c, negative flap deflection δ_f, and negative strake deflection δ_s each induce a nose-up response, i.e., positive α and q.

The α (upper) and q (lower) responses of the compensated X-29 are presented for input 1 (r_1) in Fig. 11. The compensated X-29 responds to input 1 with a positive α and negligible change in q which is the vertical translation mode discussed earlier; i.e., input 1 decouples q and θ from α. The compensated aircraft exhibits a fast response to input 1 with an α rise time of 0.125 s.

The direct lift control mode is effected by input 2 (r_2) as shown in Fig. 12. The aircraft responds to input 2 with a positive q while its α response is negligible. As with input 1, a decoupling of the aircraft responses, α and q, is observed with input 2. The aircraft q response is equally fast with a rise time of approximately 0.095 s.

A look at the control deflections shows that the flap and strake control inputs, δ_f and δ_s, respectively, control the aircraft's α response while the canard δ_c controls the q (and θ) response. A simultaneous injection of inputs 1 and 2 is necessary to effect the pitch-pointing precision control mode.

VI. Limited-Performance H_∞ Controller Design

For the high-performance solution, the control deflections consist of two consecutive large pulses at the beginning and end of the control action. The control deflections δ_c, δ_f, and δ_s for the vertical translation mode (input 1) have peak magnitudes between 80 and 172 deg which exceed the X-29's control surface deflection limits of 1) canards (leading edge): 30 deg up/60 deg down; 2) flaps (trailing edge): 10 deg up/25 deg down; and 3) strakes (trailing edge): 30 deg up and down. The control deflections are significantly less for the direct lift control mode (input 2) with peak magnitudes between 8.6 and 34 deg, and are more closely aligned with the control surface deflection limits listed above. A similar difference in control rates between inputs 1 and 2 is also observed for the compensated X-29. The peak control rates for both inputs 1 and 2, ranging from approximately 458 deg/s to over 573 deg/s, greatly exceed the X-29 actuator, minimum design requirements of 1) canards: 100 deg/s, 2) flaps: 50 deg/s, and 3) strakes: 30 deg/s.

The H_∞ synthesis of a stabilizing controller for the X-29 was reworked to bring the control surface deflections and control rates more into line with physical capabilities. A secondary objective was to retain the system robustness achieved with the initial H_∞ controller. To accomplish these objectives, a greater weighting or penalty was applied to the control input vector u by increasing the magnitude of the $W_2(s)$ ϵ term to 0.025. Although it was possible to obtain an H_∞ solution for $\gamma = 2.62$ that met the control displacement requirements, the control rates were still exceeded with this design. An H_∞ meeting all actuator specification could be obtained only with a value of $\gamma = 0.8$. A valid H_2 solution was obtained for the same conditions with $\gamma = 1$. Increasing the W_2 weighting to a higher value of 0.06 increased dramatically the control rates as the control displacements decreased. It was realized that there was an essential inconsistency in the specification of the W_1 weighting and the desire to have a solution within the actuator limitations.

Although the W_2 weighting decreases the size of the gain matrix $F(s)$, the 0-dB crossing is determined by the W_1 weighting. As the W_2 matrix is increased, the impulse-like control displacements are decreased but the control rates become large consecutive impulses at the beginning and end of the control action. Therefore, it is necessary to shift the 0-dB crossing of the W_1 weighting to the left to obtain a phys-

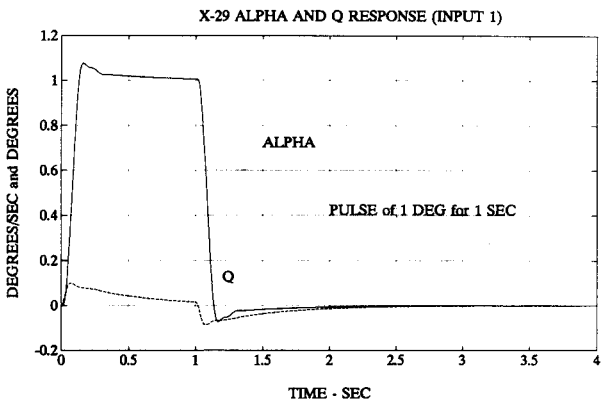

Fig. 11 Alpha and Q response (input 1).

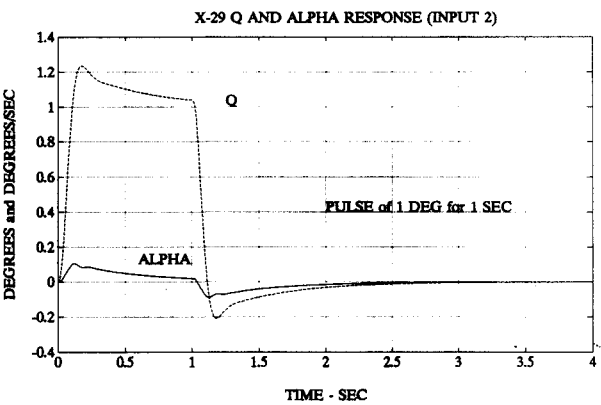

Fig. 12 Q and alpha response (input 2).

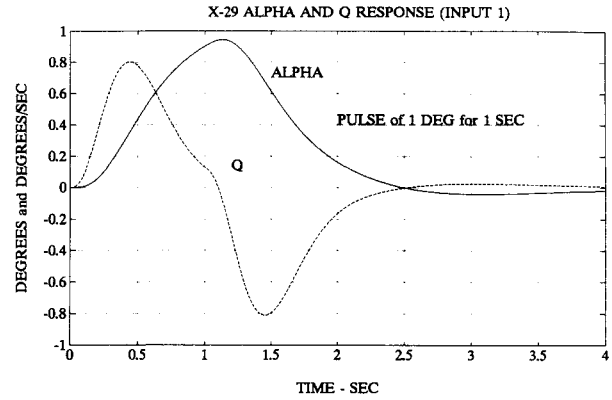

Fig. 13 Alpha and Q limited performance ($\gamma = 6$, input 1).

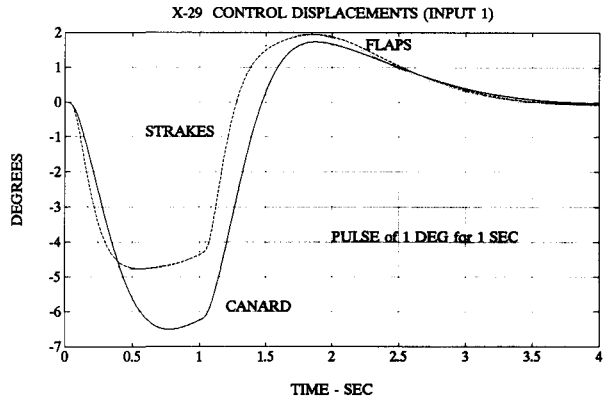

Fig. 14 Control displacements ($\gamma = 6$, input 1).

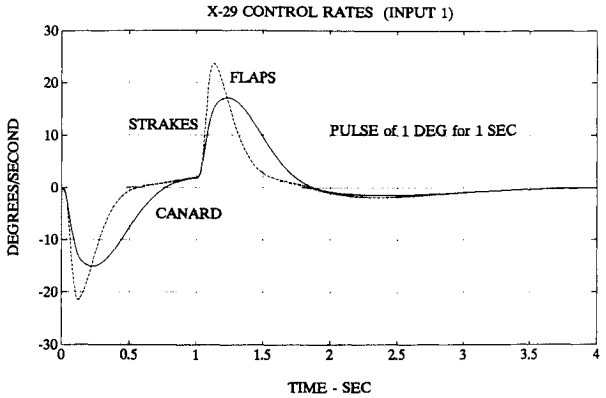

Fig. 15 Control rates ($\gamma = 6$, input 1).

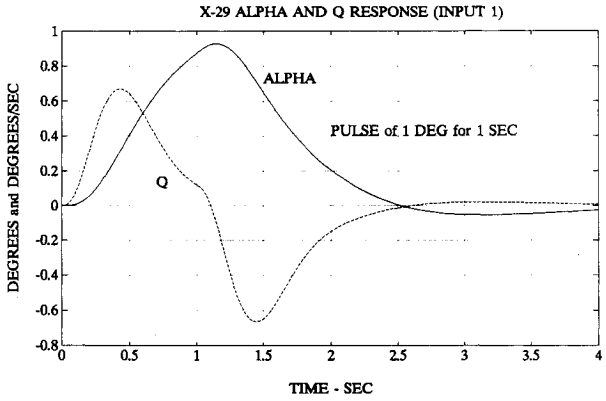

Fig. 16 Alpha and Q (H_2, $\gamma = 7$, input 1).

ically more reasonable solution. This shift was obtained by changing the numerator in Eq. (1) from 0.01 ($100s + 1$) to 0.01 ($1000s + 1$). The weighting W_2 was set at 0.028.

With a maximum achievable γ of 6.0, the limited-performance H_∞ solution for the new conditions is able to push the $\|T_{y1u1}\|_\infty$ cost function singular values to within 3.5 dB of the "all pass limit" as compared to 0.5 dB for the high-performance H_∞ solution. Comparison with the optimal performance shows that the feedback properties of the limited-performance X-29 are not as robust. The limited-performance X-29 is characterized by smaller disturbance attenuation, larger sensitivity to plant variations and modeling errors, a smaller control bandwidth, and a smaller closed-loop bandwidth. Note that, again, the unstable short-period pole of the open-loop system was mirrored into the left half-plane of the closed-loop system, i.e., -1.9539.

Identical impulse inputs of 1 deg for 1 s were applied to the limited-performance X-29 model as were previously applied to the high-performance model. Figure 13 shows the α and q response of the limited-performance X-29 for input 1. The decoupling of the α and q response as observed in the high-performance solution has been lost. This indicates that the precision flight-path modes are not achieved in the limited-performance X-29 case. The control deflections δ_c, δ_f, and δ_s for the limited-performance case are given in Fig. 14 and they are considerably smaller than those observed in the high-performance case and well within the actuator limitations. Similar observations are made for the control rates δ_c, δ_f, and δ_s for input 1 in Fig. 15. The response to input 2 were very similar except that there was a large overshoot in the Q response.

The H_2 solution for the new weightings is able to push the $\|T_{y1u1}\|_2$ cost function singular values to within 2 dB of the "all pass limit." The response to an impulse of 1 deg for 1 s on input 1 is shown in Fig. 16. The alpha response is almost identical to that of the H_∞ solution, and the Q response, although of slightly lower magnitude, has the same shape. The control displacements and control rates are also essentially identical to that of the H_∞ solution. The clear superiority of the H_∞ theory is not evident when actuator limitations are considered. In fact, the H_2 solution has a higher γ value of seven.

VII. Conclusions

In the high-performance H_∞ case ($\gamma = 12.5$), control separation or isolation is an attractive feature. In this case, the H_∞ solution achieves much better performance than that of the H_2 controller.

When realistic actuator performance is imposed on the H_∞ and H_2 controllers, separation or isolation of the control inputs is not achieved. Furthermore, the performance of the H_∞ and H_2 controllers are almost identical. The H_2 solution is, in fact, better with $\gamma = 7$.

Current modern actuator dynamics or capabilities do not support the precision flight modes characteristic of the high-performance H_∞ case.

References

[1]Chaing, R. V., and Safanov, M. G., *Robust-Control Toolbox, User's Guide,* The Mathworks, Inc., South Natick, MA, June 1988, pp. R-13–R-17.

[2]Rogers, W. L., "Applications of Modern Control Theory Synthesis to a Super-Augmented Aircraft," M.S. Dissertation, Naval Postgraduate School, Monterey, CA, June 1989.

[3]Nelson, S. W., "Development of Reduced-Order Models for Control System Design Using the OPTSYSX Program," M.S. Dissertation, Naval Postgraduate School, Monterey, CA, Dec. 1984.

[4]Gordon, V. C., "Utilization of Numerical Optimization Techniques in the Design of Multi-Input Multi-Output Control Systems," Ph.D. Dissertation, Naval Postgraduate School, Monterery, CA, Sept. 1984.